processes

MDPI

Article

Electro-Discharge Machining of $Zr_{67}Cu_{11}Ni_{10}Ti_9Be_3$: An Investigation on Hydroxyapatite Deposition and Surface Roughness

Abdul'Azeez Abdu Aliyu [1,*], Ahmad Majdi Abdul-Rani [2,*], Saeed Rubaiee [3,4], Mohd Danish [3], Michael Bryant [5], Sri Hastuty [6], Muhammad Al'Hapis Razak [7] and Sadaqat Ali [8]

1 Mechanical Engineering Department, Bayero University Kano, 700241 Kano, Nigeria
2 Mechanical Engineering Department, Universiti Teknologi PETRONAS (UTP), 32610 Seri Iskandar, Malaysia
3 Department of Mechanical and Materials Engineering, University of Jeddah, Jeddah 21589, Saudi Arabia; salrubaiee@uj.edu.sa (S.R.); mdanish@uj.edu.sa (M.D.)
4 Department of Industrial and Systems Engineering, University of Jeddah, Jeddah 21589, Saudi Arabia
5 Institute of Thermo Fluids (iTF), School of Mechanical Engineering, University of Leeds, Woodhouse Lane, Leeds LS2 9JT, UK; M.G.bryant@leeds.ac.uk
6 Mechanical Engineering Department, Universitas PERTAMINA, Jakarta 12220, Indonesia; sri.hastuty@universitaspertamina.ac.id
7 Manufacturing Section, Universiti Kuala Lumpur Malaysian Spanish Institute, Kulim Hi-Tech Park, 09000 Kedah, Malaysia; alhapis@unikl.edu.my
8 School of Mechanical & Manufacturing Engineering, National University of Sciences and Technology (NUST), Islamabad H-12, Pakistan; sadaqat.ali@smme.nust.edu.pk
* Correspondence: aaaliyu.mec@buk.edu.ng (A.A.A.); majdi@utp.edu.my (A.M.A.-R.)

Received: 23 April 2020; Accepted: 14 May 2020; Published: 26 May 2020

Abstract: This study attempts to simultaneously machine and synthesize a biomimetic nanoporous hydroxyapatite coating on the $Zr_{67}Cu_{11}Ni_{10}Ti_9Be_3$ bulk metallic glass (BMG) surface. The aim is to investigate and optimize the hydroxyapatite deposition rate and the surface roughness during the electro-discharge coating of $Zr_{67}Cu_{11}Ni_{10}Ti_9Be_3$ BMG. Scanning Electron Microscopy (SEM), X-ray powder Diffraction (XRD) and Energy-dispersive X-ray Spectroscopy (EDS) were employed to characterize and analyze the results. Response Surface Methodology using D-optimum custom design approach was utilized to generate the models and optimize the input parameters. A globule nanostructured and nanoporous coating of about 25.2 µm thick, containing mainly Ca, O, and K were ascertained. Further XRD analysis confirmed the deposition of biocompatible oxides (HA, $CaZrO_3$, and ZrO_2) and hard ZrC coating on the $Zr_{67}Cu_{11}Ni_{10}Ti_9Be_3$ BMG surface. A significant improvement in cell viability was observed in the HA electro-discharge coated BMG specimens. The numerical models for the Hydroxyapatite Deposition Rate (HDR) and Surface Roughness (SR) were developed and experimentally validated using the optimized parameters setting suggested by the software. The achieved average predicted error of 4.94 and 5.09% for the HDR and SR respectively confirmed the excellent reproducibility of the developed models.

Keywords: metallic glass; elecro-discharge; coating; hydroxyapatite; machining; optimization; deposition rate; surface roughness; RSM

1. Introduction

The liquid-like, non-crystalline (amorphous) alloy called Bulk Metallic Glass (BMG) is produced by rapid quenching of liquid melts. Unlike crystalline materials, BMG has unique properties like

high strength, high hardness, and excellent corrosion and wear resistance. This endows them with a wide range of applications. For instance, Inoue and Nishiyama [1] presented the applications of BMG as a structural, micro-sensing, and chemical materials. Although various forms of BMG were currently developed, an in-vivo study conducted by Wei, et al. [2] revealed the suitability of $Zr_{67}Cu_{11}Ni_{10}Ti_9Be_3$ BMG in producing orthopedic implants, due to its superior biocompatibility and efficient bonding to the surrounding tissues after implantation. An extensive review by Neom Eliaz [3], revealed that $Zr_{67}Cu_{11}Ni_{10}Ti_9Be_3$ BMG outweighed the current crystalline biomaterials like stainless steel, cobalt–chromium, and titanium alloys in terms of hardness, yield strength, and corrosion resistance. Moreover, they possess near-to-bone modulus of elasticity.

Some sporadically conventional techniques for shaping BMG have been documented [4]. In an end-milling of Zr-based BMG, Bakkal and Naks [5] studied the influence of the feed rate on the surface roughness, burr formation, and cutting force. A very rough surface and burr deposition were observed, especially when high feed rate is used. Han, et al. [6] investigated the cutting characteristics of the Zr-based BMG and found that, the surface morphology was greatly affected by the rate of spindle speed. However, the broad mechanical properties of the BMG resulted in the abrasion of the Diamond tool. Recently, Jiao, et al. [7] conducted experimental and numerical studies to determine the influence of laser parameters on the machining of Zr-based BMG by laser-micro machining technique. Various thermal cycles experienced by the BMG during this process make it difficult to understand the characterization that is taking place. Moreover, it still exists the issue of oxidation and crystallization which resulted in poor osteointegration of the Zr-based BMG when used as an implant. In an attempt to improve the cutability of the $Zr_{67}Cu_{11}Ni_{10}Ti_9Be_3$ BMG material without compromise to its amorphous and mechanical characteristics, researchers focused towards electro-discharge machining (EDM) technique. Yeo, et al. [8], reported the effect of the discharge energy on the burr formation, roughness, and the wear of the tool-electrode during micro-EDM of $Zr_{67}Cu_{11}Ni_{10}Ti_9Be_3$ BMG material. Reduction in the input energy produces small craters thereby reducing the burr width and the surface roughness.

The mechanisms of EDM process involved the conversion of electrical energy to the thermal energy to melt, vaporize, and remove a minute part of the workpiece material in the form of craters, after a successive spark by the flowing dielectric fluid. At this instance, the suspended metallic powder and the tool-electrode are melted, vaporized, and deposited on the workpiece surface. This resulted in the simultaneous machining and synthesis of bioceramic oxide and carbide coating on the substrate surface. Furthermore, the EDM process is proven by Axinte and Fua-Nizan [9] in producing a rough and nanoporous surface when the gas bubbles escaped during the solidification. An extensive review by Aliyu, et al. [10] and Prakash, et al. [11] reported the successful application of EDM process to shape and modify the surface of numerous biomedical materials. Ou and Wang [12] fabricated a Ti-alloy implant by EDM process and discovered a thin recast layer with enhanced roughness when 5 g/L of the bioceramic hydroxyapatite (HA) was used as the dielectric fluid additive. Aliyu, et al. [13] presented a deposition of biocompatible calcium-based oxide ($CaZrO_3$) and extremely hard carbide phases on the EDMed $Zr_{67}Cu_{11}Ni_{10}Ti_9Be_3$ BMG surface. Another study by Aliyu, et al. [14] discovered the blocking of Ni and Be by a biomimetic biocompatible rough and nanoporous coating deposited through the hydroxyapatite mixed EDM (HAm-EDM) process on the $Zr_{67}Cu_{11}Ni_{10}Ti_9Be_3$ BMG surface. Estimating the surface roughness (SR) produced during the EDM process would be helpful in implant design and manufacturing. A rough and nanostructured surface is expected to provide strong implant-tissues anchorage by enhancing the osteointegration. Hence, one of the reasons for selecting the EDM process in this research.

The above literatures revealed the capability of the EDM technique to successfully process the $Zr_{67}Cu_{11}Ni_{10}Ti_9Be_3$ BMG material. However, there are limited reports on synthesis of the hydroxyapatite coating, prediction of hydroxyapatite deposition rate (HDR), surface roughness (SR), and parameters optimization during simultaneous machining and coating of $Zr_{67}Cu_{11}Ni_{10}Ti_9Be_3$ BMG using hydroxyapatite mixed EDM (HAm-EDM) process. This study synthesized a bioactive oxide coating on the $Zr_{67}Cu_{11}Ni_{10}Ti_9Be_3$ BMG surface. Additionally, the Response Surface Methodology

using D-optimum custom design approach was employed to formulate mathematical models for the two important responses—HDR and SR. The process parameters including Peak current (P_c), Discharge duration (D_d), HA concentration (C), and tool-electrode polarity (E_p) were optimized and experimentally validated.

2. Materials and Methods

2.1. Materials

This study adopted vit1b-X $Zr_{67}Cu_{11}Ni_{10}Ti_9Be_3$ BMG produced by Materion (USA) as a workpiece (substrate) material. A 5 × 100 × 125 mm received $Zr_{67}Cu_{11}Ni_{10}Ti_9Be_3$ BMG was sliced into 5 × 9 × 10 mm pieces using wire-EDM machine to produce the workpiece specimens. The nominal compositions of the as-received BMG are 67.51 wt. % Zr, 10.61 wt. % Cu, 9.8 wt. % Ni, 3.768 wt. % Be, <1 wt. % Be and <1 wt. % Sn. A commercial titanium plate (CpTi) with size 11 × 12 × 50 mm fabricated by wire-EDM was employed as a tool-electrode. To serve as a calcium and oxygen source, a bioceramic hydroxyapatite ($Ca_5(PO4)_3(OH)$) powder 12–64 µm size was used as a dielectric fluid additive. The SEM micrograph of the as-received $Zr_{67}Cu_{11}Ni_{10}Ti_9Be_3$ BMG and the hydroxyapatite powder are shown in Figure 1. A non-distinct grain boundary in the BMG SEM micrograph shown in Figure 1a confirmed its amorphous nature and the HA particle size measurement is in Figure 1b.

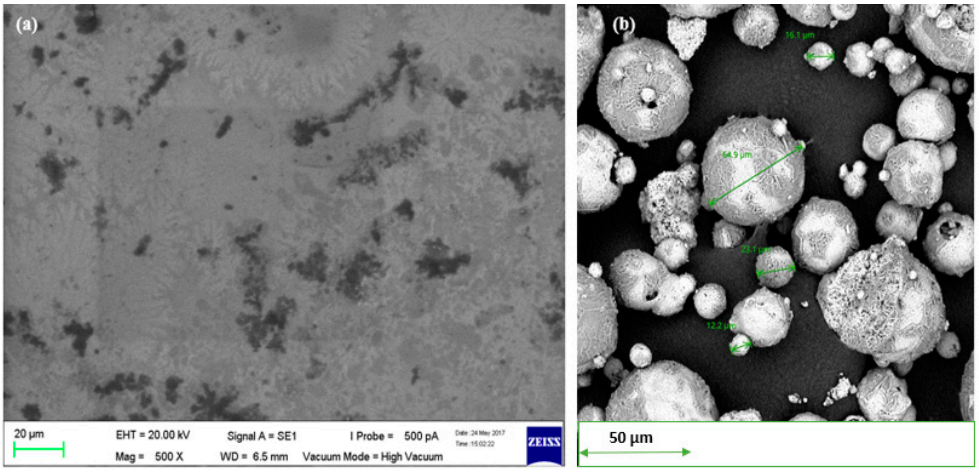

Figure 1. As-received Scanning Electron Microscopy (SEM) image: (**a**) Vit1b-X $Zr_{67}Cu_{11}Ni_{10}Ti_9Be_3$ bulk metallic glass (BMG) and (**b**) Micro-size hydroxyapatite powder.

2.2. BMG Shaping and Coating Preparation

Die-sinker EDM machine (Mitsubishi EA 60, Mitsubishi, Tokyo, Japan) was employed for simultaneous machining and coating of the $Zr_{67}Cu_{11}Ni_{10}Ti_9Be_3$ BMG workpiece material. Prior to EDM operation, the HA powder was mixed in the fabricated 200 L capacity HAm-EDM reservoir. To allow homogeneous and contentious mixing of the HA powder, 6 and 3 stirrers were employed in both HAm-EDM reservoir and the fabricated machining tank respectively. The complete experimental set-up is depicted in Figure 2. To observe the HA coating morphology and its thickness the cross-section of the HAm-EDMed $Zr_{67}Cu_{11}Ni_{10}Ti_9Be_3$ BMG specimens was grounded, polished and etched for 20 s using prepared etchant solution containing 2 mL HNO_3, 2 mL HF and 96 mL distilled water. An optical microscope (LEICA, NICON, Tokyo, Japan) was employed to observe and validate the deposition of the HA on the BMG surface, synthesized by HAm-EDM process. The specimens were further characterized using Scanning electron microscopy (SEM) (Evo LS15), X-ray powder diffraction (XRD) (X'Pert3 powder and Empyrean, PANalytical) and energy-dispersive X-ray spectroscopy (EDS) to observe the surface morphology, phases and elemental composition present in the coated specimens

respectively. The angle of 2θ (20°–90°) scanning range and 0.01 degree/step size were used during the XRD investigation.

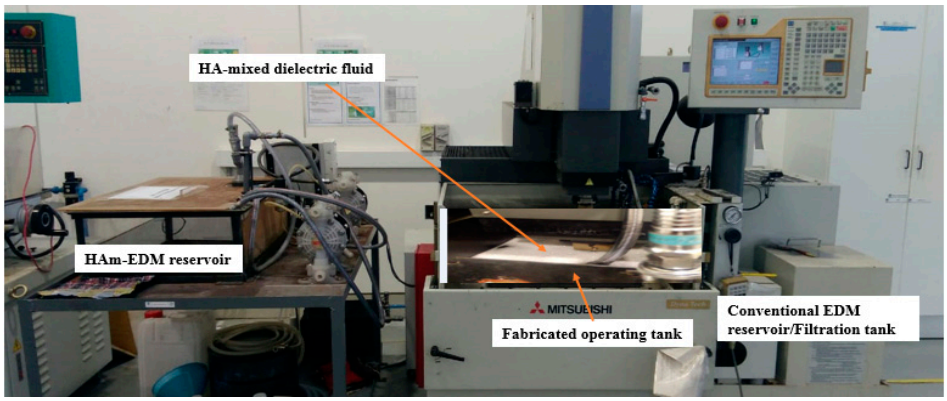

Figure 2. Hydroxyapatite mixed electro-discharge machining (EDM) (HAm-EDM) experimental set-up indicating the fabricated HAm-EDM components and the conventional EDM machine.

2.3. Screening and Optimization Experiment

Screening or fractional factorial experiment was carried out to select the best suited and most significant parameters that affect the HDR and SR. The difference of the workpiece weight after and before processing was divided by the machining time to calculate the HDR (g/min) [15]. Screening experiment was planned and analyzed using ©Minitab 18 design software. For the screening experiment, six factors which include P_c, D_d, C, E_p, Gap voltage (G_v), and Off-time (T_{off}) were selected, which are reported to have an influence on the target output (HDR and SR) [16,17]. Two level fractional factorial design (resolution IV) was conducted. Therefore, a combination of 16 experiments will be carried out. Table 1 presents the screening input parameters and experimental levels.

Table 1. Input parameters and levels for screening experiment.

Parameters	Unit	Level I	Level II
Peak current	A	5	12
Discharge duration	µs	4	16
HA concentration	g/L	5	20
Tool-electrode polarity		+	−
Off-time	µs	16	32
Gap voltage	V	10	15

To generate the model equations for predicting the HDR and SR. Response Surface Methodology through D-optimum custom design was employed in this study due to its flexibility and ability to accommodate custom models and categorical factors [18,19]. The optimized equations are written based on Equation (1). Where Y is the response variable while X1 and X2 are the independent variables. In the current study, the four factors (P_c, D_d, C, and E_p) selected from the screening experiment were used to generate empirical models and optimize the responses (HDR and SR). The selected parameters P_c, D_d, C and E_p varies at 3, 3, 4, and 2 levels respectively, with values P_c (5, 8, and 12 A), D_d (4, 8, and 16 µs), C (5, 10, 20 g/L), and E_p (Negative and Positive). The developed models will be experimentally validated, and predicated error will be calculated using Equation (2).

$$Y = f(X1) + f(X2) + \ldots \quad (1)$$

$$PE = \frac{Predicted - experimental\ values}{predicted\ value} \times 100\% \quad (2)$$

3. Results and Discussion

3.1. Hydroxyapatite Coating

Figure 3 displays the SEM image of the simultaneously shaped and coated $Zr_{67}Cu_{11}Ni_{10}Ti_9Be_3$ BMG. The HA coating of about 25.2-µm thick was deposited on the $Zr_{67}Cu_{11}Ni_{10}Ti_9Be_3$ BMG surface as observed in the cross-sectional SEM micrograph shown in Figure 3a. The electrodes and the added HA powder are melted at the point of spark during the HAm-EDM process. Thus, some of the melted HA additives and the CpTi electrode material are migrated in elemental or compound form to the BMG surface and solidified by the surrounding dielectric fluid. This produces oxides and carbide coating on the $Zr_{67}Cu_{11}Ni_{10}Ti_9Be_3$ BMG surface. Oxides are believed biocompatible and apatite inducers which promote biocompatibility of the synthetic tissues [20]. A thin recast layer of about 5.6-µm thick was also observed. At higher magnification, the HA coating microstructure shows globules nanostructured and nanoporous surface (Figure 3b). This surface is suitable for tissues in-growth into the nano-size rough and porous structure, thereby enhancing the osteointegration of $Zr_{67}Cu_{11}Ni_{10}Ti_9Be_3$ BMG as an implant. A very long peak of Ca observed in the EDS spectrum presented in Figure 4 confirmed the HA deposition on the $Zr_{67}Cu_{11}Ni_{10}Ti_9Be_3$ BMG workpiece surface. Other peaks representing K and O were also noticed. These elements are the major compositions of HA ($Ca_5(PO4)_3OH$) powder.

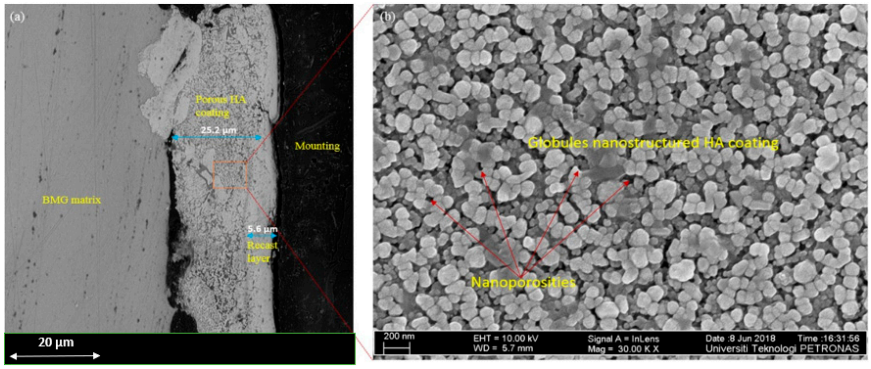

Figure 3. SEM micrograph showing: (**a**) cross-sectional micrograph of the coated $Zr_{67}Cu_{11}Ni_{10}Ti_9Be_3$ BMG by HAm-EDM process processed at P_c = 8 A, D_d = 8 µs, and C = 20 g/L and (**b**) magnified microstructural image showing the nanostructured and nanoporous hydroxyapatite (HA) coating.

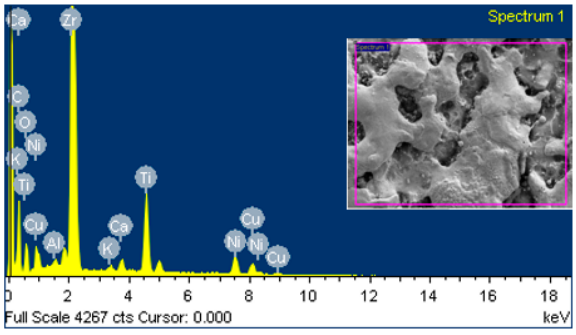

Figure 4. Energy-dispersive X-ray Spectroscopy (EDS) spectrum of the processed $Zr_{67}Cu_{11}Ni_{10}Ti_9Be_3$ BMG indicating the presence of major hydroxyapatite elements (Ca, O, and K) on the BMG surface.

The elements distribution is depicted in the elemental mapping shown in Figure 5. The elemental analysis validated the presence of the BMG (Zr and Ti) and the HA (Ca, K, and O). The mapping shows a homogeneous distribution of these elements on the coated BMG surface, except for Ca whereby some agglomeration was observed (encircled in red). The agglomeration might result due to non-uniform flushing whereby some HA are higher in some regions.

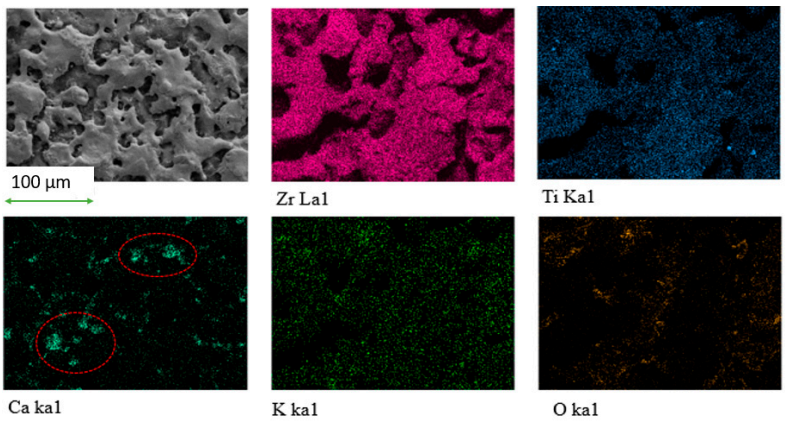

Figure 5. SEM elemental mapping showing the distribution of major $Zr_{67}Cu_{11}Ni_{10}Ti_9Be_3$ BMG and HA elements on the HAm-EDMed BMG surface. Encircled in red are deposited and agglomerated Ca element.

3.2. Phases Formation

Figure 6 displays the XRD pattern of the HA coated $Zr_{67}Cu_{11}Ni_{10}Ti_9Be_3$ BMG processed at high discharge energy (P_c = 12 A, D_d = 16 µs) and C = (5, 10, and 20 g/L). The analysis using High score software revealed various crystalline phases, including biomimetic and bioceramic biocompatible oxides (HA, $CaZrO_3$, and ZrO_2) and hard zirconium carbide. While the oxide induces the apatite formation, the carbides enhance the hardness of the HA coated BMG surface [21]. Thus, promote the biocompatibility and the strength of the BMG respectively. The oxides are formed due to the reaction of the Ca and O (in the hydroxyapatite) to the Zr (in the $Zr_{67}Cu_{11}Ni_{10}Ti_9Be_3$ BMG) workpiece material. It is obvious that some detected HA do not decompose, which might be due to poor flushing. The carbon supplied by the hydrocarbon-based dielectric fluid reacted with the Zr in BMG to produce ZrC. In a similar study, Sales et al. [22] investigated the role of calcium based oxide on the titanium alloy surface. The titanium perovskite ($CaTiO_3$) formed on the EDMed surface greatly promote the tissues growth and cells adhesion after implantation. Some unknown phases were also detected by the XRD analysis. The XRD peaks of the specimen treated through 5 g/L are sharper and longer than those coated using 10 and 20 g/L HA concentrations. Increasing the HA from 5 to 20 g/L expand the electrodes gap, thereby improving the flushing capacity, stabilizes the HAm-EDM process and hence less machining time for the crystalline peaks formation.

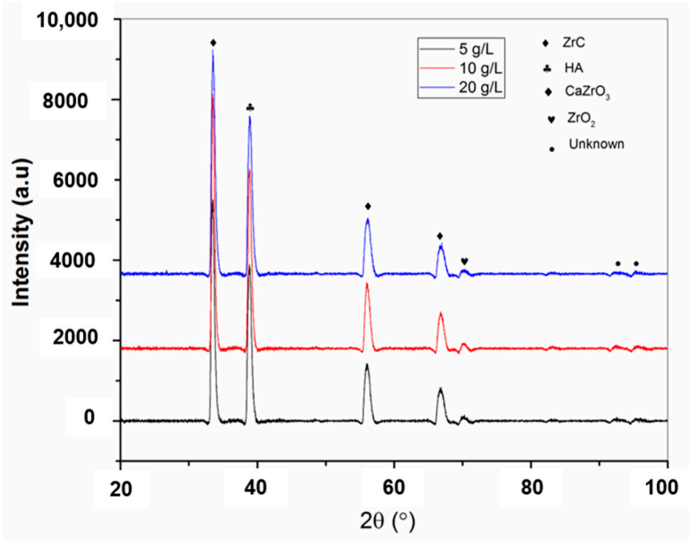

Figure 6. X-ray powder Diffraction (XRD) pattern of the coated $Zr_{67}Cu_{11}Ni_{10}Ti_9Be_3$ BMG processed at different HA concentrations indicating various oxides and carbide deposited on the BMG surface.

3.3. Effect of HA on the Surface Morphology

The SEM micrographs showing the influence of the HA concentration on the processed $Zr_{67}Cu_{11}Ni_{10}Ti_9Be_3$ BMG surface is depicted in Figure 7. Numerous craters, microcracks, and porosities (encircled in red) could be observed in a specimen processed by EDM as seen in Figure 7a. The addition of 5 g/L HA produces a smoother surface with less cracks and shallower craters (Figure 7b). Some droplets which might occur due to less gap flushing were also noticed in the craters. The surface tends to be smoother when the HA concentration further increased to 15 g/L (Figure 7c). In addition, no cracks and less craters were noticed. The surface changes to a dendritic nanostructured and nanoporous coating when 20 g/L of HA powder was used (Figure 7d). Hydroxyapatite powder reduces the surface roughness by enlarging the machining gap, increases flushing capacity and stabilizes the HAm-EDM process. A similar result was achieved when HA powder was added to the dielectric fluid during EDM of β-titanium implant [23].

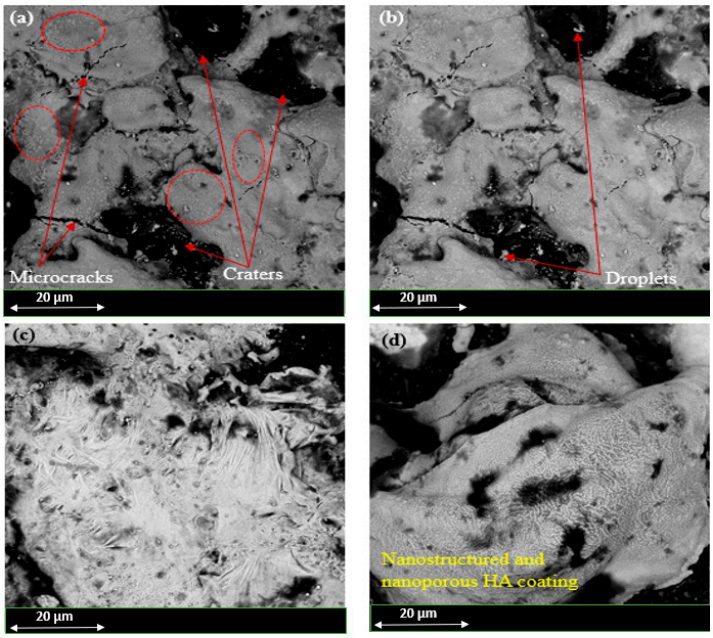

Figure 7. SEM micrographs of the $Zr_{67}Cu_{11}Ni_{10}Ti_9Be_3$ BMG processed at constant P_c = 8 A and D_d = 8 µs while varying the HA powder concentration: (**a**) 0 g/L, (**b**) 5 g/L, (**c**) 15 g/L, and (**d**) 20 g/L.

3.4. Screening Results Analysis

EDM machine has a wide range of parameters which might be influential to the responses HDR and SR. Based on the machine capability and literature survey six parameters including P_c, D_d, C, E_p, G_v, and T_{off} were selected for the screening experiment. A two-level fractional factorial (resolution IV) which gives a total of 16 experiments was used. The values of the HDR and SR were calculated and analysed to determine the most significant factors and the interactions. The normal plot and Pareto chart for the HDR presented in Figure 8a,b depicted that P_c, D_d, C, and E_p are the most significant factors on the HDR. Moreover, the interactions E_pC and P_cC were also found significant as observed in the Pareto chart for the HDR. Similarly, the factors P_c, D_d, C, E_p, and interaction D_dC were found to have an influence on the SR as observed in the normal plot and Pareto chart of the SR shown in Figure 8c,d, respectively. Additionally, the factor D_d was found to have a major influence on the SR as confirmed by the Pareto chart. Generally, the factors G_v, T_{off} and/or their interactions were insignificant on both the HDR and SR. Therefore, these two non-significant factors were dropped, and hence further design of experiment (DOE) will only consider four significant factors including P_c, D_d, C, and E_p. The parameters obtained in this study were in agreement with those achieved when shaping siliconized silicon carbide in an aluminium powder mixed dielectric fluid [24].

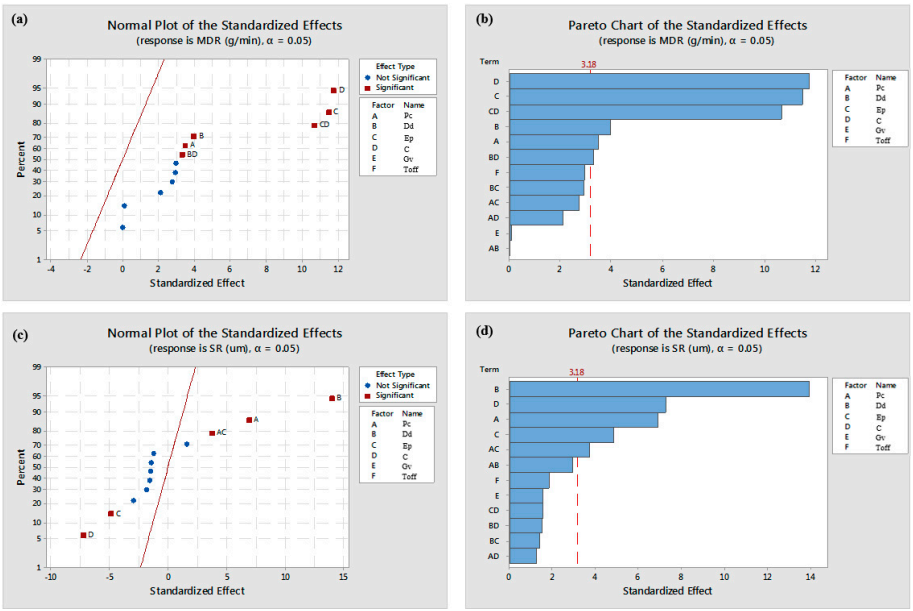

Figure 8. Screening experimental results showing the most significant parameters and insignificant parameters in the normal plot and Pareto chart of Hydroxyapatite Deposition Rate (HDR) and Surface Roughness (SR). All the factors extended beyond the red line in the Pareto chart are significant while those below the line are considered insignificant.

3.5. Modelling and Optimization of HDR and SR

D-optimal design is a response surface methodology which generates a design that best estimate the influence of the process parameters particularly suited for screening studies [18]. Four factors, including P_c, D_d, C, and E_p and mixed level was used to achieve a total of 24 experiments. Table 2 displays the DOE matrix and the data for the selected responses, HDR and SR.

Table 2. Design of experiment (DOE) matrix and Experimental results for the HDR.

Std Order	Run Order	P_c (A)	D_d (µs)	C (g/L)	E_p	HDR (g/min)	SR (µm)
17	1	5	16	5	+	0.00067	4.342
18	2	8	16	10	+	0.00072	9.953
5	3	12	8	10	−	0.00081	8.183
1	4	5	4	5	−	0.00019	2.292
4	5	8	8	10	−	0.00094	3.337
7	6	8	4	20	−	0.0014	1.782
22	7	5	16	20	+	0.00144	3.830
21	8	12	4	20	+	0.0075	3.802
19	9	12	16	10	+	0.00036	26.623
23	10	5	16	20	+	0.00194	5.404
12	11	12	16	20	−	0.00022	5.800
11	12	12	8	20	−	0.00089	5.327
10	13	5	8	20	−	0.0022	4.040
24	14	12	16	20	+	0.00078	22.662
3	15	12	16	5	−	0.00027	18.381
20	16	5	4	15	+	0.0011	3.102
16	17	8	8	5	+	0.00071	6.361
14	18	12	4	5	+	0.00056	24.33
13	19	5	4	5	+	0.00024	7.101
2	20	12	16	5	−	0.00028	18.959
15	21	12	4	5	+	0.00035	24.330
9	22	5	8	20	−	0.0025	1.618
6	23	5	16	10	−	0.00067	4.592
8	24	8	4	20	−	0.0016	1.854

The contribution of each parameter on the HDR is indicated in the ANOVA shown in Table 3. The model value of 0.0001 ("Prob > F") justifies its significance. The table also shows that the factors P_c, D_d, C, E_p, and interactions AB, AD, BC, CD, and B^2 with "Prob > F" values less than 0.05 are significant terms. The lack of fit "Prob > F" of 0.2170 indicates its insignificance. The model is required to fit the response (HDR), therefore it is good for the lack of fit to be non-significance.

Table 3. ANOVA for quadratic model of the hydroxyapatite deposition rate.

Source	Sum of Squares	df	Mean Square	*F* Value	*p*-Value Prob > F	
Model	17.82	13	1.37	26.35	<0.0001	**significant**
A-P_c	0.39	1	0.39	7.52	0.0208	
B-D_d	0.42	1	0.42	8.15	0.0171	
C-C	6.24	1	6.24	119.9	<0.0001	
D-E_p	1.67	1	1.67	32.17	0.0002	
AB	1.49	1	1.49	28.67	0.0003	
AC	0.066	1	0.066	1.26	0.2875	
AD	0.35	1	0.35	6.81	0.0261	
BC	2.56	1	2.56	49.15	<0.0001	
BD	0.082	1	0.082	1.57	0.2383	
CD	1.07	1	1.07	20.58	0.0011	
A2	0.086	1	0.086	1.65	0.2286	
B2	1.38	1	1.38	26.51	0.0004	
C2	0.055	1	0.055	1.06	0.3268	
Residual	0.52	10	0.052			
Lack of Fit	0.35	5	0.071	2.1	0.217	**not significant**
Pure Error	0.17	5	0.034			
Cor Total	18.34	23				

The analysis of variance (ANOVA) for the SR is depicted in Table 4. The regression model, significant factors, interactions and lack of fit tests are summarized by the ANOVA table. Model and the model terms with less than 0.05 "prob > F" are regarded as significant terms 18. Therefore, from the ANOVA table the model and the factors P_c, D_d, C, and E_p are considered the significant terms of the SR. The model is expected to fit, because the lack of fit "prob > F" value of 0.2213 indicates its non-significance.

Table 4. ANOVA for linear model of the surface roughness.

Source	Sum of Squares	df	Mean Square	*F* Value	*p*-Value Prob > F	
Model	14.66	4	3.67	21.63	<0.0001	**Significant**
A-P_c	6.78	1	6.78	40.03	<0.0001	
B-D_d	1.64	1	1.64	9.67	0.0058	
C-C	2.37	1	2.37	13.96	0.0014	
D-E_p	1.84	1	1.84	10.85	0.0038	
Residual	3.22	19	0.17			
Lack of Fit	2.74	14	0.2	2.04	0.2213	**not significant**
Pure Error	0.48	5	0.096			
Cor Total	17.88	23				

The normal probability of the residuals and the residuals versus run plots for the HDR and SR are depicted in Figure 9. The normal plots for both HDR and SR shows that the data lies within the straight line as seen in Figure 9a,b respectively. This confirmed that the selected terms are only the significant factors and the errors are normally distributed. In the residuals versus run plots for HDR and SR presented in Figure 9c,d respectively, all the studentized residuals of regression lie within the required limit (±3 sigma), and not any outliers observed. This confirmed the capability of the model to predict the responses.

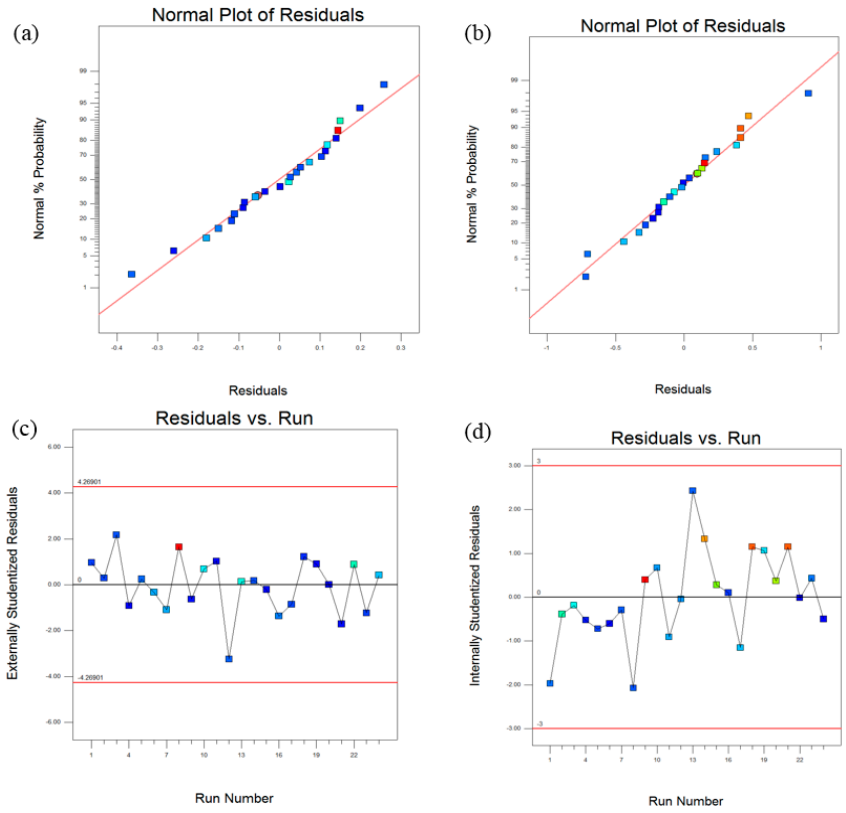

Figure 9. Normal plots of residuals: (**a**) HDR and (**b**) SR and Residuals versus Runs plots for: (**a**) HDR and (**b**) SR.

A curved plot 3D surface plots for the HDR and SR are presented in Figure 10. The curves surface observed in the HDR plots (Figure 10a–c) indicated the significance of the curvature and a quadratic model. The highest HDR is observed at 10 A and 8 µs parameters setting in the current versus discharge time 3D surface plot shown in Figure 10a. Moreover, the C versus P_c plot shows highest HDR of 0.002 g/min at C = 20 g/L and P_c = 5 A as observed Figure 10b. A similar HDR is achieved when C = 20 g/L and D_d = 8 µs parameters setting was employed as shown in Figure 10c. The influence of P_c and D_d on the SR is presented in the 3D surface plot shown in Figure 10d. A flat surface which indicated insignificant curvature is observed. From this plot, it can be noticed that the SR increases with increases in both P_c and D_d. Therefore, higher SR can be observed at P_c = 12 A and D_d = 16 µs while the lowest SR can be achieved at P_c = 5 A and D_d = 4µs parameters setting.

The ANOVA table presented produces the equation which relates the responses HDR and SR to the input parameters. The final predicted model equations in terms of the actual factors for HDR and SR are presented in Equations (3)–(6).

When E_p = Negative:

$$Ln(HDR) = -12.25099 + 0.35873 \times P_c + 0.66913 \times D_d + 0.11239 \times C - 0.016032 \times P_c \times D_d - 2.56623 \times 10^{-3} \times P_c \times C - 0.010376 \times D_d \times C - 0.014847 \times P_c^2 - 0.020995 \times D_d^2 + 2.47001 \times 10^{-3} \times C^2 \quad (3)$$

When E_p = positive:

$$Ln(HDR) = -12.96631 + 0.44302 \times P_c + 0.64098 \times D_d + 0.18750 \times C - 0.16032 \times P_c \times D_d - 2.56623 \times 10^{-3} \times P_c \times C - 0.010376 \times D_d \times C - 0.014847 \times P_c^2 - 0.020995 \times D_d^2 + 2.47001 \times 10^{-3} \times C^2 \quad (4)$$

When E_p = negative:

$$Ln(SR) = +0.19857 + 0.17168 \times P_c + 0.049622 \times D_d - 0.048342 \times C \quad (5)$$

When E_p = positive:

$$Ln(SR) = +0.76123 + 0.17168 \times P_c + 0.049622 \times D_d - 0.048342 \times C \quad (6)$$

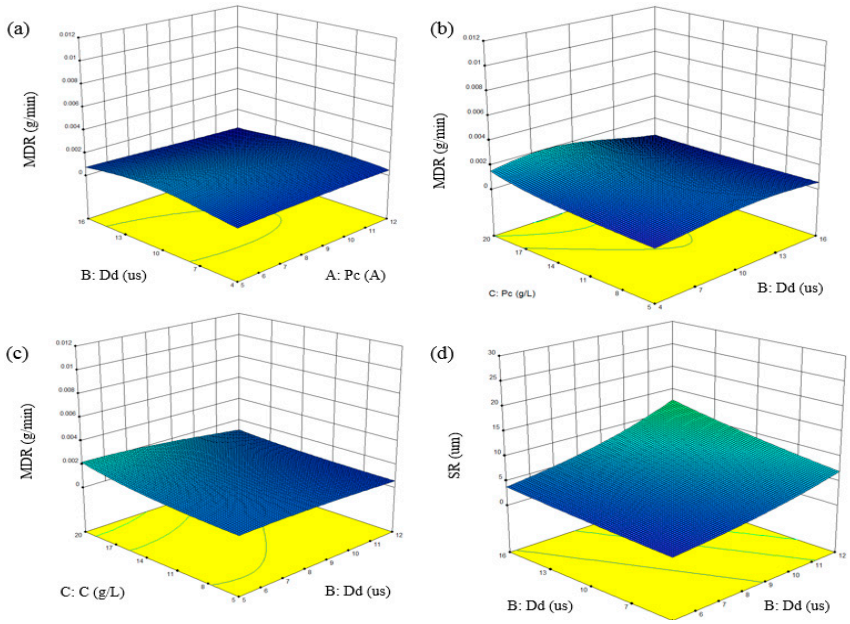

Figure 10. 3D surface plots for HDR and SR.

Table 5 shows the model summary statistic for HDR. The software recommended a quadratic model for the HDR, due to its least standard deviation (0.23), largest statistic R-square (0.7710), and lowest Predicated Error Sum of Squares (PRESS) (4.20) compared to the linear model.

Table 5. Model summary statistic for HDR.

Source	Std. Dev.	R-Squared	AdjustedR-Squared	PredictedR-Squared	PRESS	
Linear	0.64	0.5788	0.4901	0.2712	13.37	
2FI	0.39	0.8918	0.8085	0.5517	8.22	
Quadratic	0.23	0.9716	0.9348	0.771	4.2	**Suggested**
Cubic	0.18	0.9909	0.9579		+	Aliased

The model summary statistic for the SR is shown in Table 6. It could be observed that the linear model for SR is suggested by the design expert software for the SR. This is due to its least standard deviation of 0.41, largest statistic (predicted) R-square of 0.7000 and lower Predicated Error Sum of Squares (PRESS) of 5.36 as required.

Table 6. Model summary statistic for SR.

Source	Std. Dev.	R-Squared	AdjustedR-Squared	PredictedR-Squared	PRESS	
Linear	0.41	0.8199	0.782	0.7	5.36	**Suggested**
2FI	0.35	0.911	0.8426	0.5191	8.6	
Quadratic	0.37	0.9242	0.8257	0.2428	13.54	
Cubic	0.31	0.9732	0.8767		+	Aliased

The response optimization can be directly obtained from the design expert software by considering the response value and desirability. The software suggests the optimum parameters combination for maximizing HDR and minimizing SR. The solutions suggested by the software for maximizing HDR and minimizing SR are presented in Tables 7 and 8.

Table 7. Solutions for maximizing HDR suggested by the software.

Number	P_c	D_d	C	E_p	HDR	Desirability	
1	9.081	7.227	19.973	+	0.008	1	**Selected**
2	9.302	6.492	19.996	+	0.008	1	
3	10.415	6.703	19.997	+	0.008	1	
4	10.261	5.904	20	+	0.008	1	
5	9.705	6.963	19.953	+	0.008	1	

Table 8. Suggested solutions for minimizing SR.

Number	P_c	D_d	C	E_p	SR	Desirability	
1	5.016	4.568	19.23	−	1.55	1	**Selected**
2	5.007	4.584	19.434	−	1.533	1	
3	5.142	4.742	19.066	−	1.61	1	
4	5.346	4.625	19.794	−	1.601	1	
5	5.034	4.878	19.76	−	1.539	1	

Following a successful selection of the input parameters' optimum level, a confirmatory test was conducted to validate the numerical model developed for the responses HDR and SR. In this study, the optimum parameters recommended by the design software was used to conduct the confirmation test. Thus, it will be possible to establish the adequacy of the achieved numerical models. Optimum parameters setting plays a significant role not only in improving the quality but also in the industries by reducing parts production time and cost. This study planned to achieve a maximum rate of hydroxyapatite deposition and minimum surface roughness (nanostructured surface). Using the optimum parameters conditions generated by the software, five sets of confirmatory tests were carried out. The results of both responses are presented in Table 9.

Table 9. Confirmation test results at optimized input parameters.

Run Order	P_c (A)	D_d (µs)	E_p	C (g/L)	SR (µm)	HDR (g/min)
1	8.0	7.0	+	20	4.325	0.00693
2	8.0	7.0	+	20	4.809	0.00701
3	8.0	7.0	+	20	4.4642	0.00712
4	8.0	7.0	+	20	5.038	0.00718
5	8.0	7.0	+	20	5.092	0.00687

The five sets of results for the HDR and SR provided by the software (predicated) and those conducted at optimum parameters setting (actual experiment) were compared in Table 10.

Table 10. Result comparison for predicated and experimental HDR and SR.

Run Order	Experimental SR (µm)	Predicated SR (µm)	Percentage Error (%)	Experimental HDR (g/min)	Predicated HDR (g/min)	Percentage Error (%)
1	5.092	5.033	1.17	0.00693	0.00739	5.82
2	4.809	5.011	4.03	0.00701	0.00738	5.01
3	4.642	5.053	8.10	0.00712	0.00740	3.78
4	5.038	5.011	0.53	0.00718	0.00739	2.84
5	5.690	5.095	11.6	0.00687	0.00741	7.29
Average prediction error (%)			5.09			4.94

To enable accurate estimation of the predicted models, prediction error (PE) of each response was determined. The average error of the five results was also calculated to achieve the average PE (APE). The PE is calculated through Equation (1). The APE for HDR and SR was found to be 4.94% and 5.09%, respectively. A study conducted by Mir et al. [25] and Aliyu et al. [26] reported that an APE of less than 10% confirmed the excellent reproducibility of the experimental conclusions. Therefore, the APE of 4.95% (HDR) and 5.09% (SR) in this study can be considered to be within the acceptable limit.

4. Conclusions

The main conclusions of this study are as follows:

- HAm-EDM process can be used to synthesize a novel biomimetic biocompatible oxide and carbide coatings on the $Zr_{67}Cu_{11}Ni_{10}Ti_9Be_3$ BMG surface.
- The experimental result revealed a HA coating containing mainly biocompatible oxides and hard carbide of 25.2-µm thickness, synthesized on the $Zr_{67}Cu_{11}Ni_{10}Ti_9Be_3$ BMG material by HAm-EDM process. The main hydroxyapatite elements (Ca, O, and K) were found deposited on the HAm-EDMed $Zr_{67}Cu_{11}Ni_{10}Ti_9Be_3$ BMG surface.
- The model equations for both HDR and SR were successfully developed. Furthermore, the optimum parameters setting for minimizing SR and maximizing HDR are achieved. The predicted error of both SR and HDR was found to be 5.09% and 4.94% respectively. Therefore, the errors were considered within the acceptable limit.

Author Contributions: Conceptualization, A.A.A.; Formal analysis, A.A.A.; Funding acquisition, A.M.A.-R., S.R. and M.D.; Methodology, A.A.A.; Project administration, A.M.A.-R.; Resources, S.H., and A.A.A.; Supervision, A.M.A.-R. and M.B.; Writing—original draft, A.A.A.; Writing—review & editing, S.A., S.R., M.D., and M.A.R. All authors have read and agreed to the published version of the manuscript.

Funding: This research was funded by YUTP- Research grant (015LC0-164) and "University of Jeddah, Jeddah, Saudi Arabia".

Acknowledgments: The authors appreciated the financial support by University of Jeddah, Jeddah, Saudi Arabia /Universiti Teknologi PETRONAS International Collaborative Research for supporting this research.

Conflicts of Interest: The authors declare no conflict of interest.

References

1. Inoue, A.; Nishiyama, N. New bulk metallic glasses for applications as magnetic-sensing, chemical, and structural materials. *MRS Bullatin* **2007**, *32*, 651–658. [CrossRef]
2. Wei, S.; Weiqi, G.; Hongjun, A. The In Vivo Evaluation of the Biocompatibility and Bone Bonding Efficiency of Zr-Based Bulk Metallic Glass Implant Material. *J. Biomert. Tissue Eng.* **2018**, *8*, 1464–1468. [CrossRef]
3. Eliaz, N. Corrosion of Metallic Biomaterials: A Review. *Materials* **2019**, *12*, 407. [CrossRef] [PubMed]
4. Axinte, E.; Bofu, A.; Wang, Y. An overview on the conventional and nonconventional methods for manufacturing the metallic glasses. *MATEC Web Conf. EDP Sci.* **2017**, 03003. [CrossRef]
5. Bakkal, M.; Nakş ler, V. Cutting mechanics of bulk metallic glass materials on meso-end milling. *Mater. Manuf. Process.* **2009**, *24*, 1249–1255. [CrossRef]
6. Han, D.; Wang, G.; Li, J.; Chan, K.; To, S.; Wu, F.; Gao, Y.; Zhai, Q. Cutting characteristics of Zr-based bulk metallic glass. *J. Mater. Sci. Tech.* **2015**, *31*, 153–158. [CrossRef]
7. Jiao, Y.; Brousseau, E.; Han, Q.; Zhu, H.; Bigot, S. Investigations in nanosecond laser micromachining on the Zr52.8Cu17.6Ni14.8Al9.9Ti4.9 bulk metallic glass: Experimental and theoretical study. *J. Mater. Process. Tech.* **2019**, *273*, 116232. [CrossRef]
8. Yeo, S.H.; Tan, P.C.; Aligiri, E.; Tor, S.B.; Loh, N.H. Processing of zirconium-based bulk metallic glass (BMG) using micro electrical discharge machining (Micro-EDM). *Mater. Manuf. Process.* **2009**, *24*, 1242–1248. [CrossRef]
9. Axinte, E.; Fua-Nizan, R. Investigation of nanoporosities fabricated on metallic glass surface by hydroxyapatite mixed EDM for orthopedic application. *Malays. J. Fundl. Appl. Sci.* **2017**, *13*, 523–528.

10. Aliyu, A.A.A.; Abdul-Rani, A.M.; Ginta, T.L.; Prakash, C.; Axinte, E.; Razak, M.A.; Ali, S. A Review of Additive Mixed-Electric Discharge Machining: Current Status and Future Perspectives for Surface Modification of Biomedical Implants. *Adv. Mater. Sci. Eng.* **2017**, *2017*. [CrossRef]
11. Prakash, C.; Kansal, H.; Pabla, B.; Puri, S. Electric dischargemachining—A potential choice for surface modification of metallic implants for orthopedic applications: A review. *J. Eng. Manuf.* **2015**, *230*, 331–353. [CrossRef]
12. Ou, S.-F.; Wang, C.-Y. Effects of bioceramic particles in dielectric of powder-mixed electrical discharge machining on machining and surface characteristics of titanium alloys. *J. Mater. Process. Tech.* **2017**, *245*, 70–79. [CrossRef]
13. Aliyu, A.A.A.; Abdul-Rani, A.M.; Ginta, T.L.; Rao, T.; Selvamurugan, N.; Roy, S. Hydroxyapatite mixed-electro discharge formation of bioceramic Lakargiite ($CaZrO_3$) on Zr–Cu–Ni–Ti–Be for orthopedic application. *Mater. Manuf. Process.* **2018**, *33*, 1734–1744. [CrossRef]
14. Aliyu, A.A.A.; Abdul-Rani, A.M.; Rao, T.V.V.L.N.; Axinte, E.; Hastuty, S.; Parameswari, R.P.; Subramaniam, J.R.; Thyagarajan, S.P. Characterization, adhesion strength and in-vitro cytotoxicity investigation of hydroxyapatite coating synthesized on Zr-based BMG by electro discharge process. *Surf. Coat. Tech.* **2019**, *370*, 213–226. [CrossRef]
15. Rahang, M.; Patowari, P.K. Parametric optimization for selective surface modification in EDM using Taguchi analysis. *Mater. Manuf. Process.* **2016**, *31*, 422–431. [CrossRef]
16. Ahmed, A. Deposition and analysis of composite coating on aluminum using Ti–B4C powder metallurgy tools in EDM. *Mater. Manuf. Process.* **2016**, *31*, 467–474. [CrossRef]
17. Watane, K.H.; Gudadhe, M. Enhancement of Surface Hardness of Cutting Tools by Surface Coating Using EDM. *Int. J. Mech. Eng. Infor. Tech.* **2014**, *2*, 614–630.
18. Montgomery, D.C. *Design and Analysis of Experiments*; John Wiley & Sons: New York City, NY, USA, 2017.
19. Danish, M.; Yahya, S.M.; Saha, B.B. Modelling and optimization of thermophysical properties of aqueous titania nanofluid using response surface methodology. *J. Therm. Anal. Calorim.* **2019**, 1–13. [CrossRef]
20. Popescu, M.; Manolea, O.; Diaconu, A.; Mercuţ, V. Zirconia Biocompatibility in Animal Studies—A Systematic Review. *Mater. Tech. Dent.* **2017**, *376*, 12–28. [CrossRef]
21. Ahmad, M.A.; Abdul Azeez, A.A.; Sri, H.; Turnad, L.G.; Rao, T.V.V.L.N.; Ali, S. Enhancing surface quality of Zr-Cu-Ni-Ti-Be through hydroxyapatite mixed EDM for potential orthopedic application. In *AIP Conference Proceedings*; AIP Publishing LLC.: Kuala Lumpur, Malaysia, 2018; Volume 2035, p. 080010. [CrossRef]
22. Sales, W.F.; Oliveira, A.R.F.; Raslan, A.A. Titanium perovskite ($CaTiO_3$) formation in Ti6Al4V alloy using the electrical discharge machining process for biomedical applications. *Surf. Coat. Technol.* **2016**, *307 Pt A*, 1011–1015. [CrossRef]
23. Chander, P.; Uddin, M.S. Surface modification of β-phase Ti implant by hydroaxyapatite mixed electric discharge machining to enhance the corrosion resistance and in-vitro bioactivity. *Surf. Coat. Technol.* **2017**, *326 Pt A*, 134–145.
24. Aliyu, A.A.; Hamidon, M.; Rohani, J.M. Parametric Study Of Powder Mixed Electrical Discharge Machining And Mathematical Modeling of SiSiC Using Copper Electrode. *Proc. Adv. Mater. Res.* **2014**, *845*, 878–882. [CrossRef]
25. Mir, M.J.; Sheikh, K.; Singh, B.; Malhotra, N. Modeling and analysis of machining parameters for surface roughness in powder mixed EDM using RSM approach. *Int. J. Eng. Sci. Tech.* **2012**, *4*, 45–52. [CrossRef]
26. Aliyu, A.A.; Rohani, J.M.; Abdul Rani, A.M.; Musa, H. Optimization of Electrical Discharge Machining Parameters of SiSiC through Respons Surface Methodology. *J. Teknol.* **2017**, *79*, 119–129.